DOI: 10.21062/mft.2024.055 © 2024 Manufacturing Technology. All rights reserved. http://www.journalmt.com

Analysis and Experimental Verification of Human-Robot Coupling Collaboration Characteristics for Lower Extremity Exoskeleton Rehabilitation Robot Based on ADAMS

Peiqin Wang (0009-0009-7345-9510)[1], Hui Song (0009-0004-6254-1539)[1], Runqiang Liu (0009-0004-4119-9025)[1], Yunchun Jiang (0009-0000-6876-5171)[1], Yi Zheng (0000-0002-7853-8279)[1,2*]
[1]Institute of Intelligent Manufacturing, Qingdao Huanghai University, Qingdao, Shandong, 266427, China. Email: 55051207@qq.com; song123456hui@163.com; 305154583@qq.com; 180392761@qq.com
[2]School of Mechanical and Automotive Engineering, Qingdao University of Technology, Qingdao, 266520, China. Email: fw.2004@163.com

Motor rehabilitation contributes to neural remodeling in individuals with motor disabilities, which is crucial for their recovery of motor ability. In addressing the No. of human-machine coupling and synergistic motion characteristics in motor rehabilitation, this study analyzes the collaborative motion characteristics of each joint in the lower limbs. A virtual human-machine coupling system is proposed, and the driving functions of the human-machine coupling system are designed. By utilizing ADAMS motion simulation software, the motion characteristics of the human-machine system are analyzed, and the variation patterns of motion parameters at key positions are obtained. Based on this, the system's synergy is analyzed and experimentally validated from the perspectives of gait, motion speed, and joint motion angles. The experimental results demonstrate that the hip and knee joint angles of the exoskeleton robot exhibit a motion pattern highly consistent with that of the human body, with an angle error of less than 3° indicating excellent synergy.

Keywords: Exoskeleton Rehabilitation Robot, Human-Machine Coupling, ADAMSIntroduction

1 Introduction

As the pace of life accelerates and work-related stress increases, diseases are trending towards affecting younger individuals. Stroke is a major cause of lower limb disability, and its incidence has been steadily rising [1]. However, with advancements in medical technology, the mortality rate has significantly decreased. Nevertheless, the incidence rate remains high. As of October 2021, there were over 28 million stroke patients in China. Approximately 90% of stroke patients experience lower limb motor impairments, requiring long-term rehabilitation training [2-4]. This significantly impacts the quality of life for both patients and their families and places a heavy economic burden on them.

Currently, traditional rehabilitation methods mainly rely on rehabilitation therapists and passive rehabilitation devices. The effectiveness of rehabilitation largely depends on the therapist's experience and expertise, with only 40%-50% of patients showing noticeable improvement[5-7]. Additionally, the rehabilitation process is repetitive and monotonous, posing significant challenges in terms of manpower and finances. Independent lower limb gait recovery is the ultimate rehabilitation goal for individuals with lower limb motor impairments. With the rapid development of rehabilitation medical technology in China, there has been a diversification of rehabilitation methods and an emphasis on proactive approaches[8-10].

Therefore, lower limb exoskeleton rehabilitation robots, with the goal of improving patients' quality of life, primarily focus on the reconstruction, training, and adaptation of motor function in individuals with lower limb motor impairments. Thus, their role in replacing traditional human-assisted passive rehabilitation methods is an inevitable trend.

To address No.s related to the coordination and synchronization of movement between rehabilitation equipment and patients, this paper analyzes the collaborative movement characteristics from the perspective of human-machine coupling. It includes an analysis of collaborative movements in virtual scenarios and experimental verification using an optical motion capture system.

2 Development of a Virtual Prototype for Human-Machine Coupling System

From a simulation analysis perspective, the model structure was simplified [11-12]. Additionally, to simulate a realistic human-machine system walking environment, a ground model was constructed under the exoskeleton's sole. The completed human-machine system model in ADAMS is depicted in Fig 1.

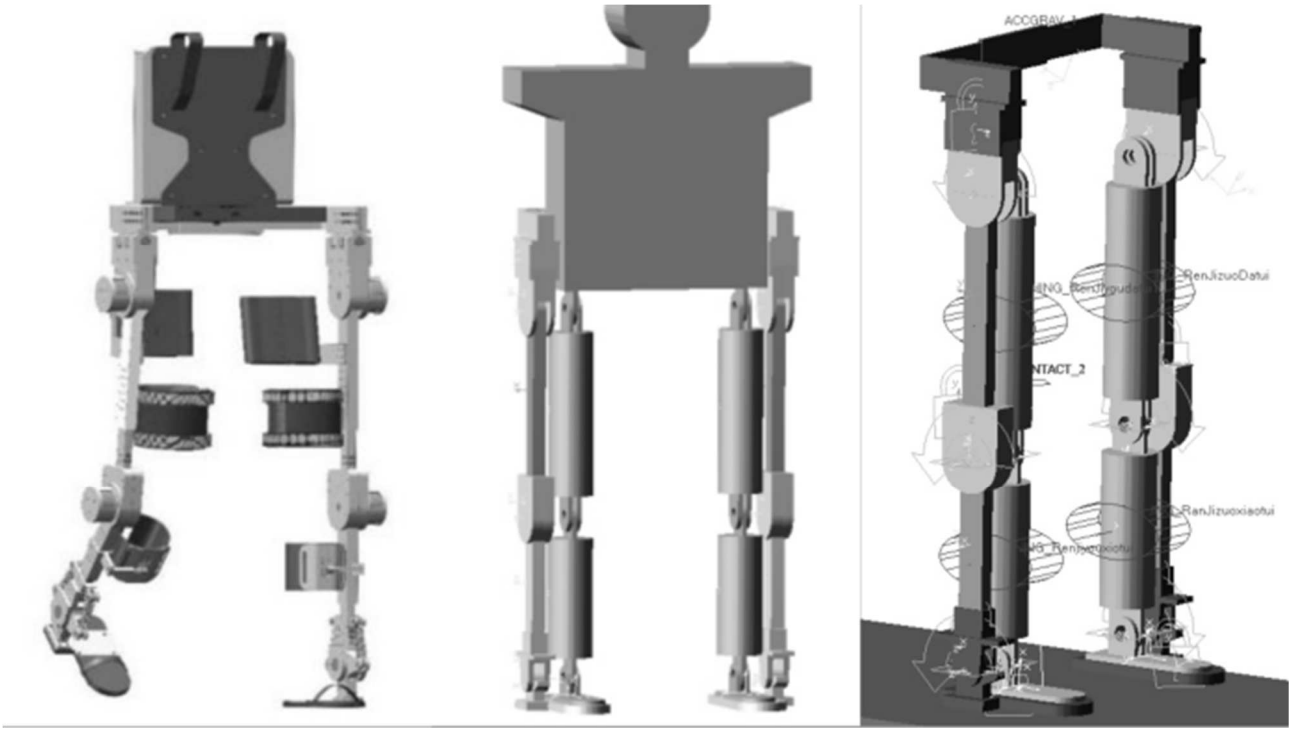

Fig. 1 *Prototype Model and Simplified Human-Machine System Model in ADAMS*

Incorporating respective attributes for the human body, exoskeleton, and ground, a STEP function was employed as the driving function[13-15]:

$$STEP(x, x_0, h_0, x_1, h_1) \tag{1}$$

Where 'x' represents the variable; 'x0' and 'x1' are the initial and final values; 'h0' and 'h1' represent the initial and final function values of 'x0' and 'x1'.

In the ADAMS View module, the virtual prototype of the exoskeleton robot is depicted in Fig 1.

Where,the left hip joint's driving function:

$$STEP(time,0,0,0.55,-42d) + STEP(time,0.55,0,0.9,42d) + STEP(time,0.9,0,1,-5d) \tag{2}$$

Left knee joint's driving function:

$$STEP(time,0,0,0.15,-16d) + STEP(time,0.15,0,0.4,15d) + STEP(time,0.4,0,0.75,-55d) + STEP(time,0.75,0,1,56d) \tag{3}$$

Right hip joint's driving function:

$$STEP(time,0,0,0.3,39d) + STEP(time,0.4,0,0.9,-42d) + STEP(time,0.9,0,1,3d) \tag{4}$$

Right knee joint's driving function:

$$STEP(time,0,0,0.15,-30d) + STEP(time,0.15,0,0.4,15d) + STEP(time,0.4,0,0.75,-55d) + STEP(time,0.75,0,1,60d) \tag{5}$$

Set the simulation time to 2 seconds with 1000 steps, and initialize the simulation in a standing posture. This will provide the motion characteristics of the exoskeleton robot within one gait cycle.

3 Exoskeleton Robot Simulation Results Analysis

Simulating the displacement and velocity of key components involved in lower limb motion, we first analyze the changes in the position and velocity of the center of mass of the lower limb rehabilitation robot. The curves depicting the changes in the Y and Z directions of the left thigh's center of mass position are shown in Fig 2.

From Fig 2, it can be observed that the center of mass position of the left thigh in the Y-direction exhibits periodic fluctuations, with a range of approximately -0.465m to -0.38m. The center of mass velocity reaches its maximum at 0.6 seconds, with an instantaneous velocity close to -0.45m/s, indicating the time when the thigh is at its highest point before descending. Afterward, there is no significant fluctuation in the motion, and the mechanism operates relatively smoothly.

In the Z-direction, the center of mass position varies in the range of -0.25m to 0.55m within one gait cycle, showing a trend of initially descending and then ascending, indicating an overall forward motion of the center of mass. The center of mass velocity reaches its

maximum at 0.8 seconds, with an instantaneous velocity ranging from approximately -0.2m/s to 0.45m/s.

The curves depicting the center of mass position in the Y and Z directions of the right calf are shown in Fig 3.

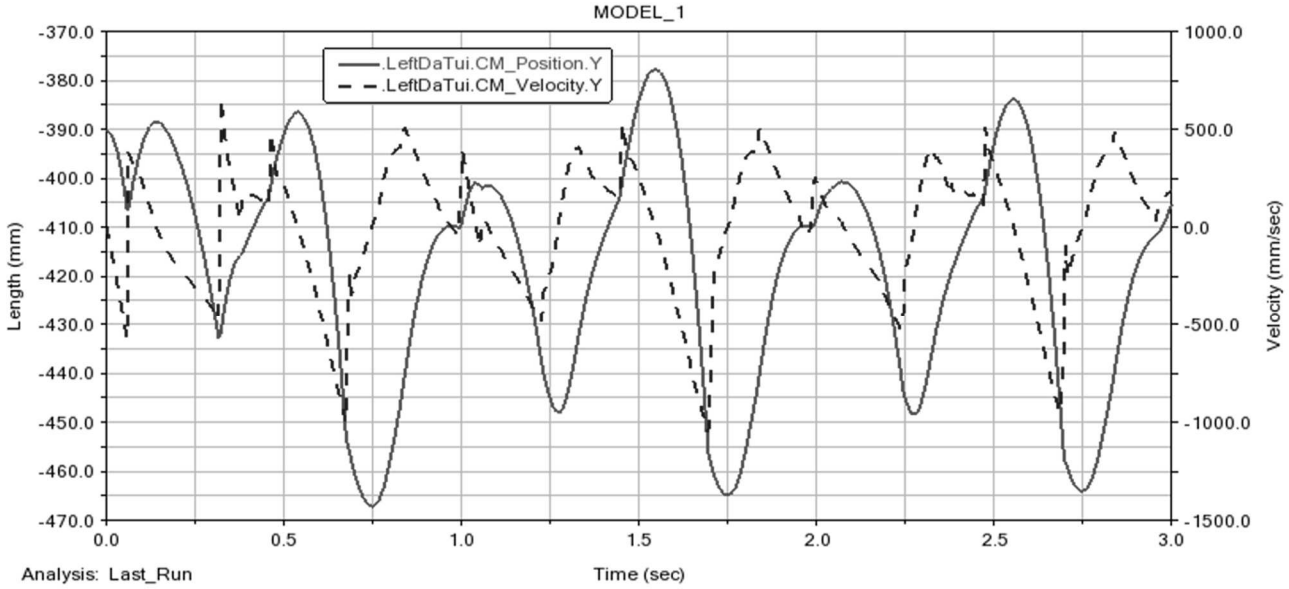

(a)Y direction

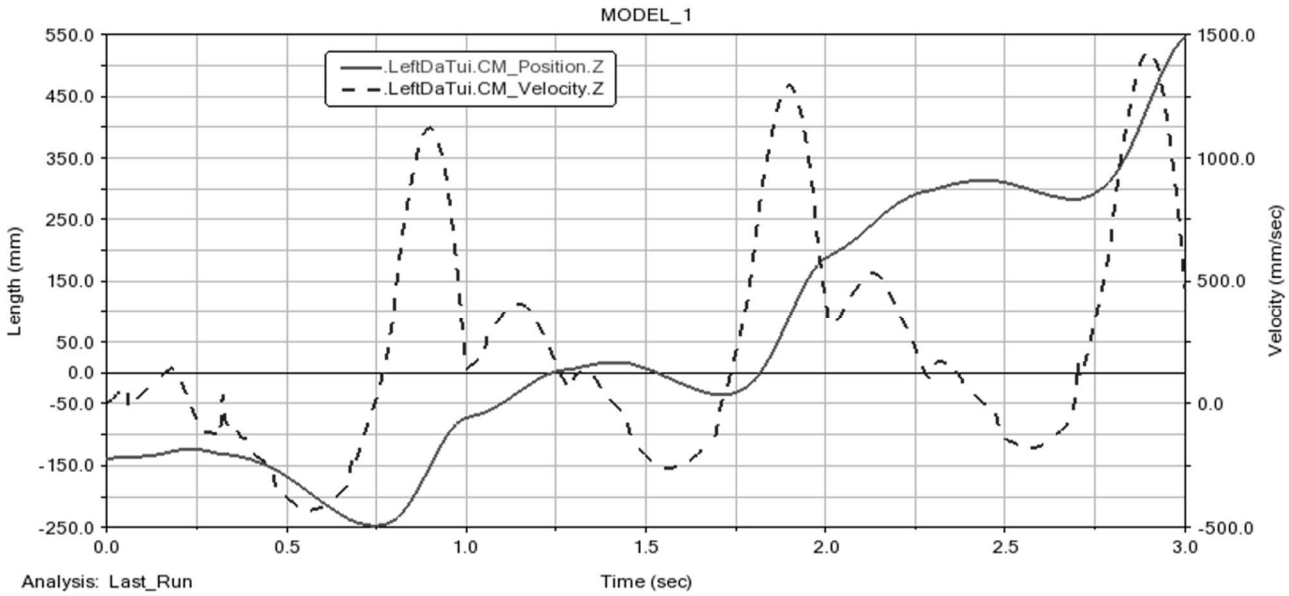

(b)Z direction

Fig. 2 *Schematic Representation of Left Thigh Movement in the Exoskeleton*

In Fig 3(a): The overall trend of the center of mass position of the calf in the Y-direction in Figure 5(a) exhibits an initial increase followed by a decrease, with a range of approximately -0.86 m to 0.74 m. The center of mass velocity varies within the range of -0.88 m/s to 0.8 m/s.

In Fig 3(b): The center of mass position in the Z-direction of the calf varies in the range of -0.25 m to 0.55 m within one gait cycle, showing a trend of initially descending and then ascending, indicating an overall forward motion of the center of mass. The center of mass velocity reaches its maximum at 0.5 seconds, with an instantaneous velocity close to 0.8 m/s, ranging from approximately -0.75 m/s to 0.9 m/s.

From the curves in the figure, it can be observed that the center of mass velocity curve of the calf exhibits more pronounced fluctuations compared to the thigh, mainly because the calf follows the swinging motion of the thigh, resulting in a more complex trajectory. The calf's movement trajectory effectively reflects the smoothness of the mechanism's operation.

The curves depicting the center of mass position in the ankle-foot region are shown in Fig 4.

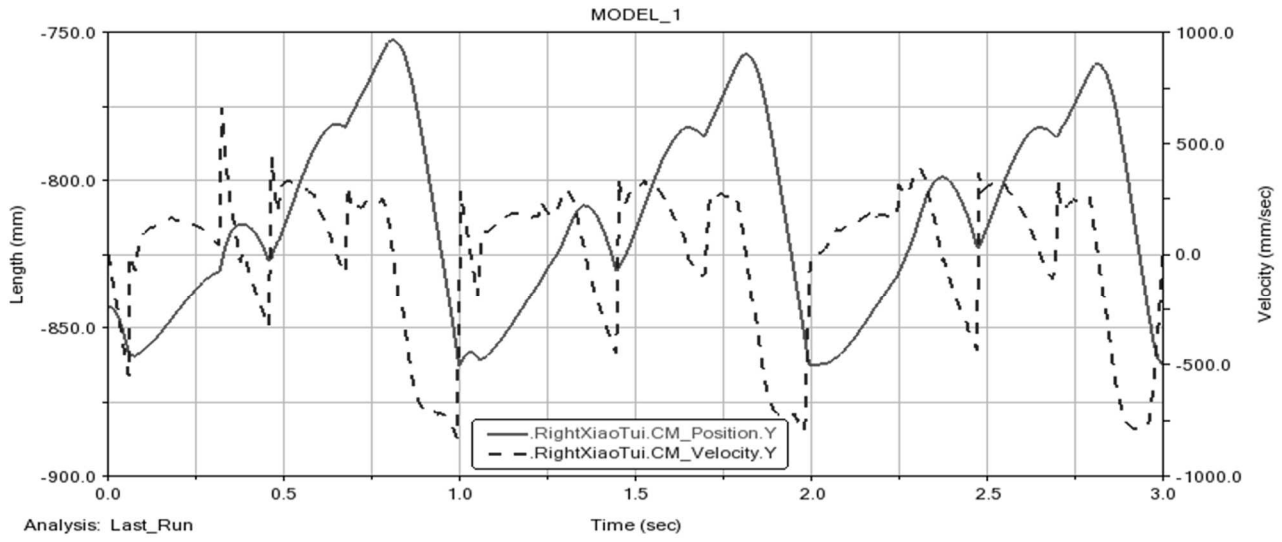

(a) Y direction

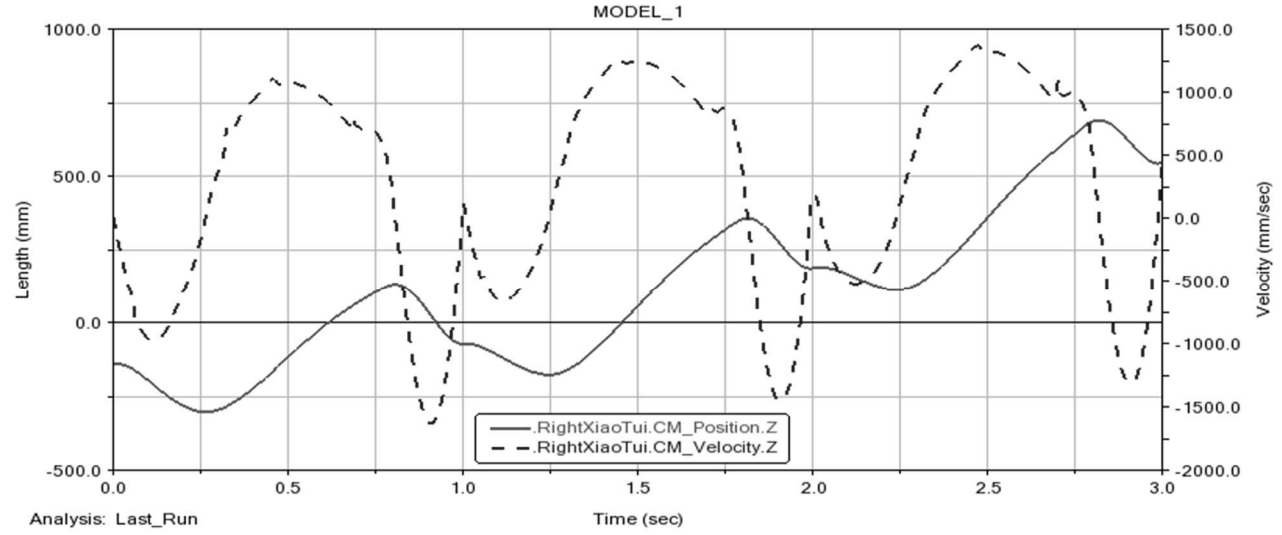

(b)Z direction

Fig. 3 *Center of Mass Position of the Right Calf in the Exoskeleton*

In Fig 4(a), the center of mass position of the foot in the Y-direction shows an upward trend, descending from 0.75s to 1s before entering the next gait cycle. The range of center of mass position variation in the Y-direction is approximately -1.14m to -1m. The foot's center of mass velocity exhibits significant changes between 0.75s and 1s, ranging from -1.12m/s to -0.98m/s, while the velocity changes are relatively small in other phases.

In Fig 4(b), the center of mass position of the foot in the Z-direction generally shows an upward trend. Within the first gait cycle, it varies in the range of -0.25m to 0.25m. This includes a backward swing from 0s to 0.25s and a forward swing to the landing phase from 0.25s to 1s. The center of mass velocity undergoes significant changes between 0.75s and 1s, ranging from -0.4m/s to 1m/s. Notably, between 0.75s and 0.1s, there are substantial changes in both horizontal and vertical velocity, indicating a critical role of the lower limb's foot movement during this phase. To maintain the exoskeleton robot's stability while moving forward, the foot's center of mass velocity also continuously changes over time. The curves in the figure show that the exoskeleton foot's movement is generally consistent with the desired preset trajectory.

Overall, the curves representing the changes in the center of mass positions of the thighs and feet are smooth, indicating the smooth operation of the exoskeleton robot. This suggests that the designed exoskeleton robot can meet the needs of human-machine cooperative movement. Throughout the process, there are no significant abnormal fluctuations, except for a minor range of fluctuations at the beginning of the simulation due to momentary movements and the transition between left and right leg phases.

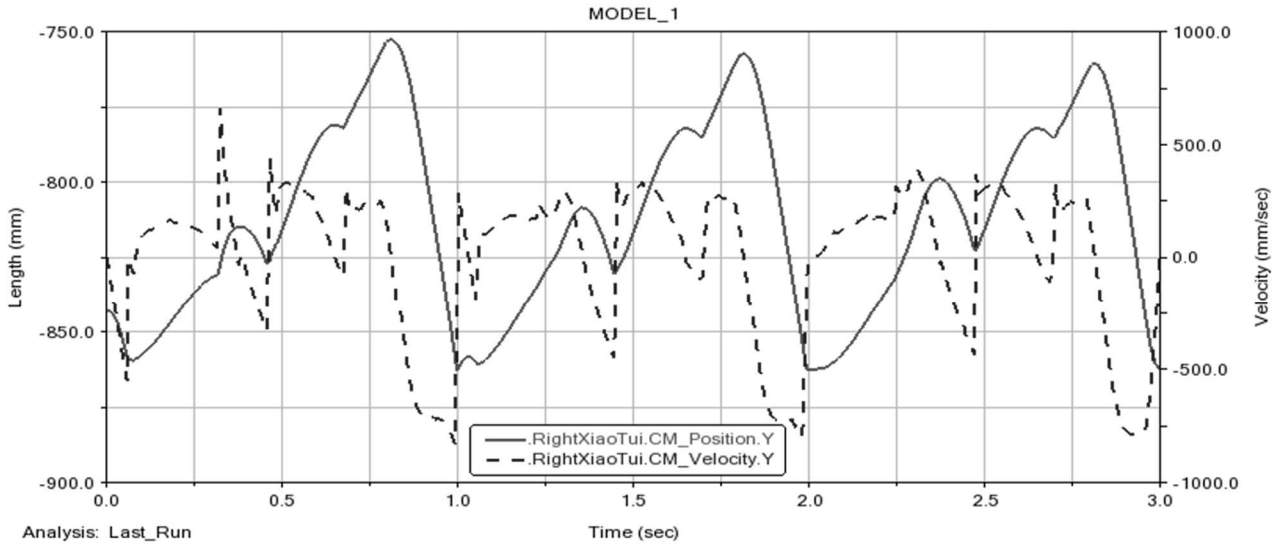

(a) Y direction

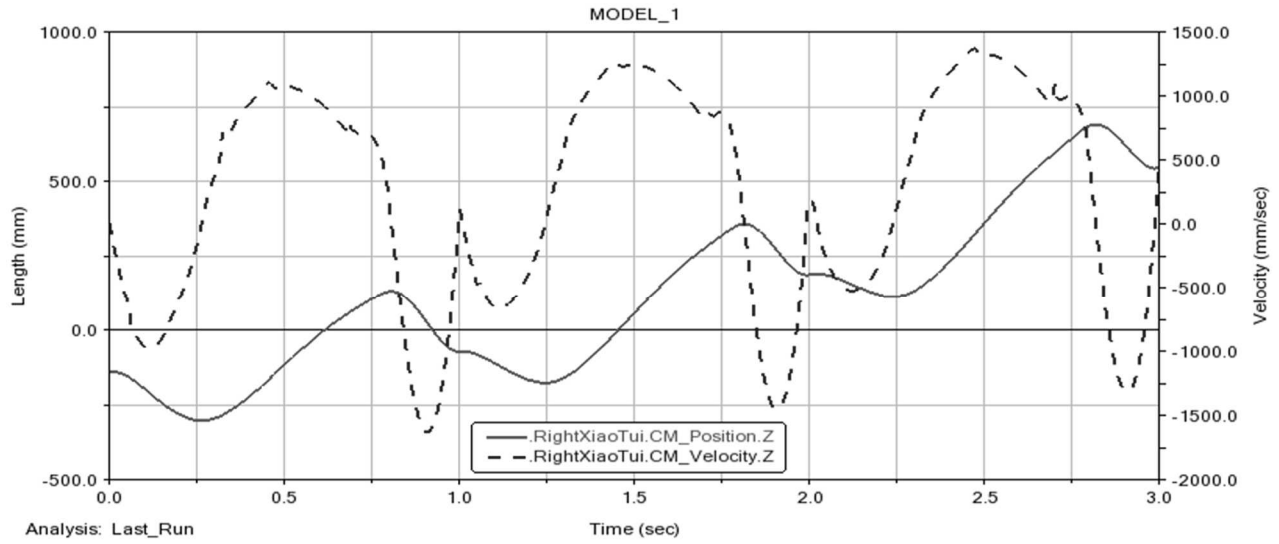

(b) Z direction

Fig. 4 *Center of Mass Position of the Right Ankle-Foot Region in the Exoskeleton*

4 Human-Machine Coupling System Synergy Analysis

4.1 Gait Analysis of the Human-Machine Coupling System

In the simulation control, pre-resetting was performed with 1000 steps and a simulation time of 2 seconds, followed by the initiation of the simulation. In the post-processing window, animation was loaded with foot center-of-mass points marked as trajectory markers. The settings for the motion trails were configured with 3 frames for ghosting and a 100% decay rate. The simulation results depict the lower limb gait motion, as shown in Fig 5.

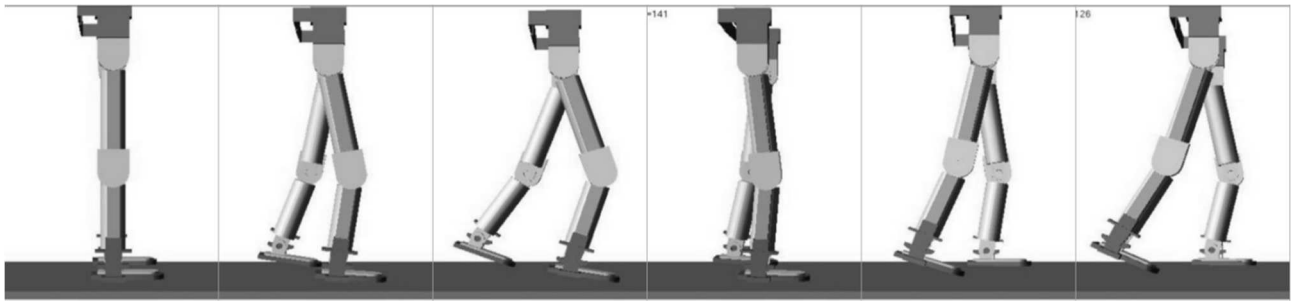

Fig. 5 *Schematic Representation of the Walking Process in the Simulation*

From Fig 5, we can observe the motion of the human-machine system throughout a complete gait cycle. The first three frames depict the right leg in the support phase, while the left leg moves from the moment of contact with the ground to swinging backward. The following three frames show the right leg in the support phase, with the left leg swinging backward before transitioning to forward swing. By observing the motion simulation process, it is evident that the human body model can walk in synchronization with the exoskeleton robot's movement. Additionally, the motion of the exoskeleton robot and the human lower limbs at various joints appears smooth, without any interference or simulation failures, indicating the system's excellent tracking capability.

4.2 Synergy Analysis of System Movement Velocities

A comparison of the center of mass velocities of the human-machine exoskeleton system for the thighs is shown in Figure 6. In this figure, the red curve represents the motion trajectory of the exoskeleton mechanism, the blue curve represents the motion trajectory of the human lower limbs, and the pink curve represents the deviation between the two.

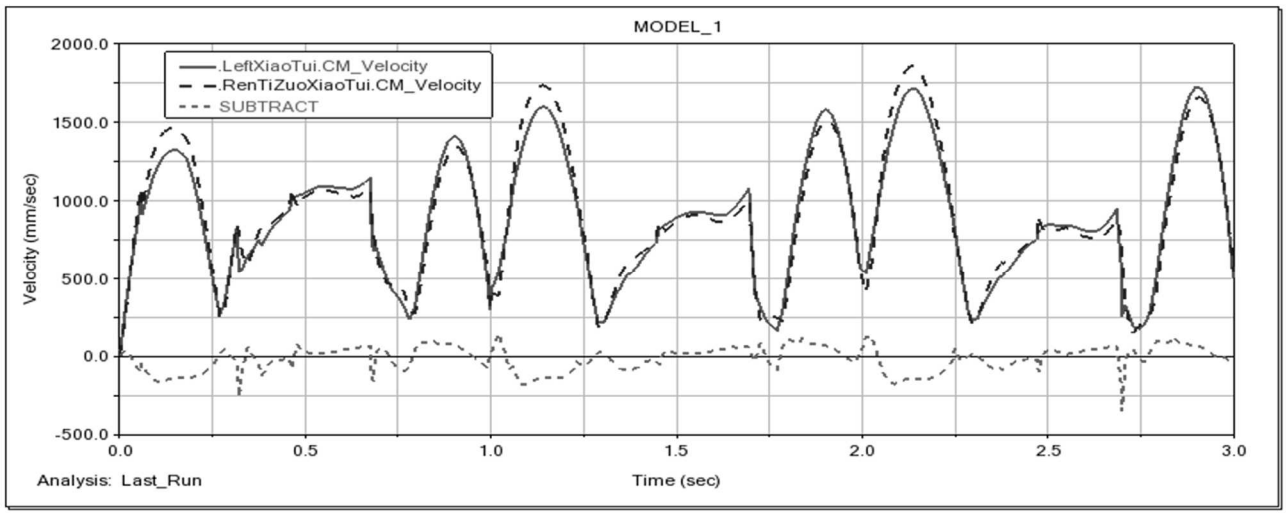

(a)Velocity Change Curve of the Calf's Center of Mass

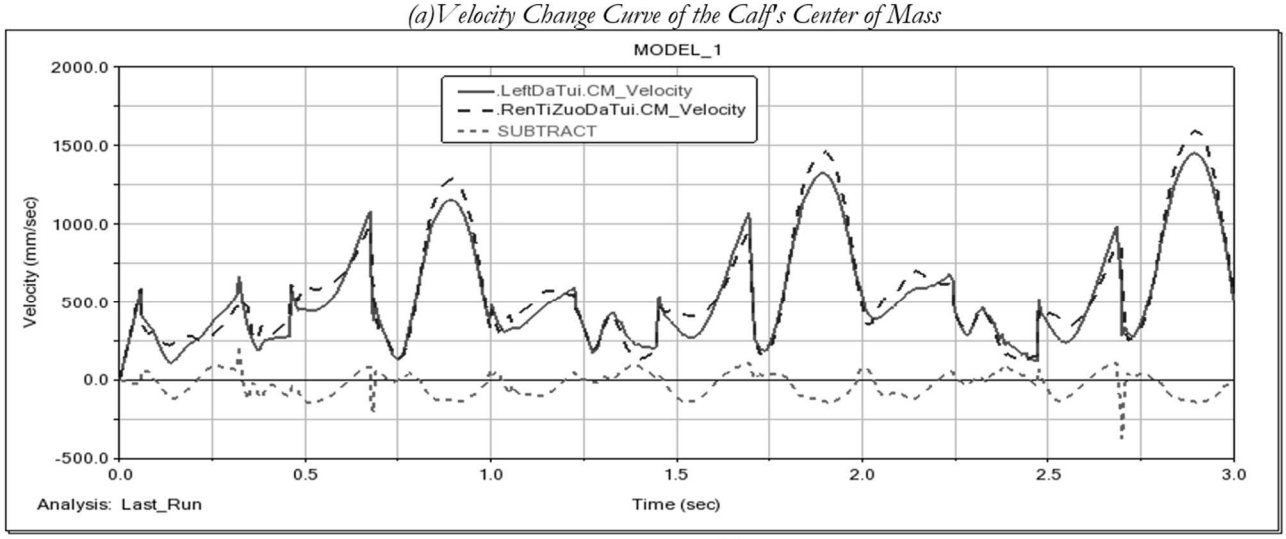

(b)Velocity Change Curve of the Thigh's Center of Mass

Fig. 6 *Comparison of Center of Mass Velocities for the Thighs in the Human-Machine Exoskeleton System*

From Fig 6, it can be observed that in the simulation results, there is a continuous difference between the center of mass velocities of the exoskeleton's and human's thighs, and this difference varies over time. Both velocities follow a consistent pattern, with the maximum difference occurring at 2.7 seconds, reaching 0.25m/s. In other phases, the differences are relatively small. This suggests that in terms of lower limb movement speed, the human-machine system maintains good synergy.

4.3 Synergy Analysis of Joint Angles in the System

A comparison of the joint angles for the human-machine exoskeleton system is shown in Fig. 7. In this figure, the red curve represents the motion trajectory

of the exoskeleton mechanism, the blue curve represents the motion trajectory of the human lower limbs, and the pink curve represents the deviation between the two.

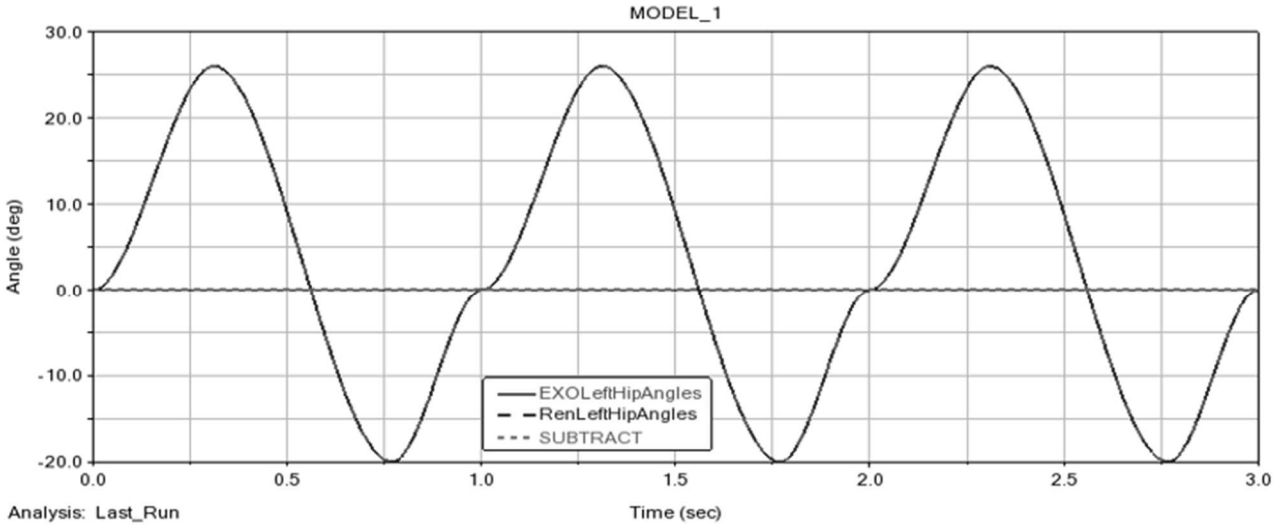

(a) hip joint

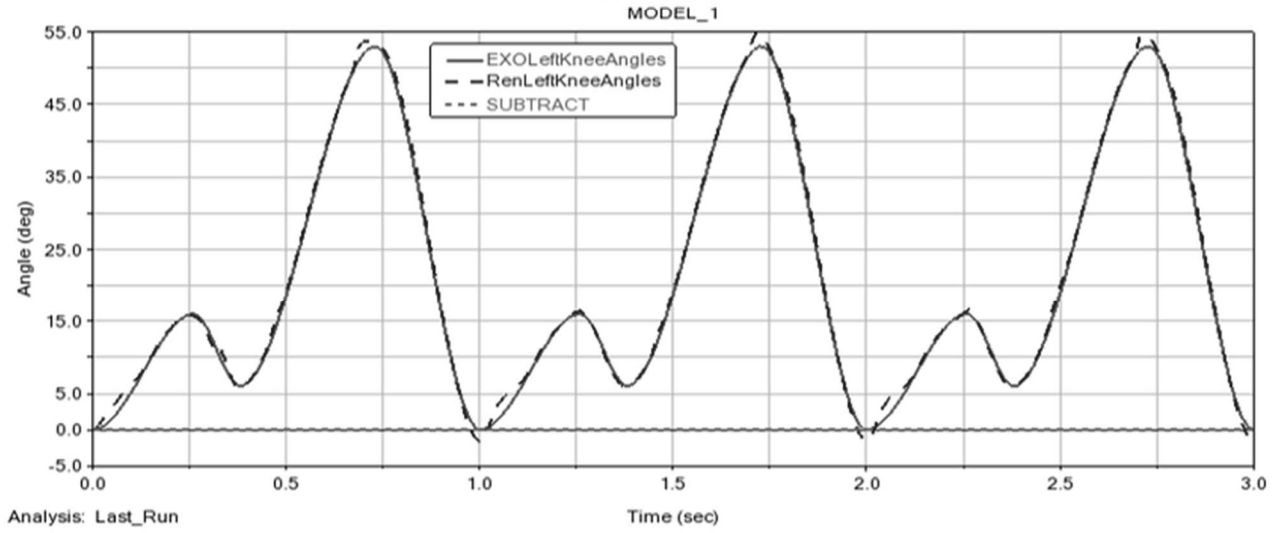

(b) knee joint

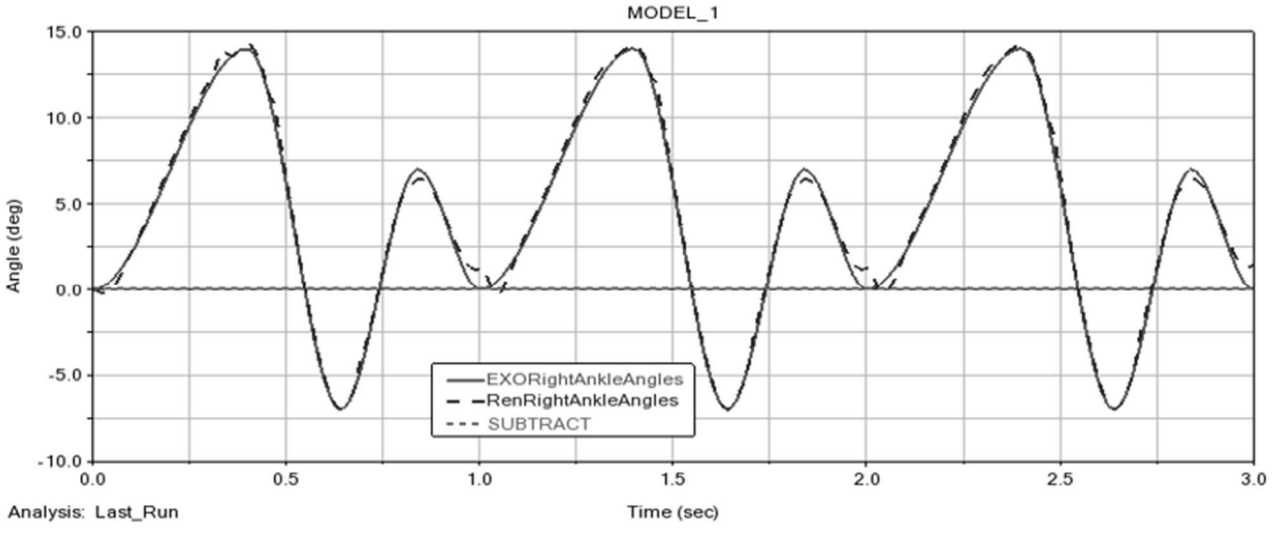

(c) ankle joint

Fig. 7 *Comparison of Joint Angles between the Human and Exoskeleton in the Human-Machine Exoskeleton System*

From Fig 7, it can be observed that the range of hip joint angles is -20° to 26° ,knee joint angles range from 0° to 55° ,and ankle joint angles vary between -7° to 14° .In the 01s phase, it is in the swing phase. During this phase, the right leg's hip joint rapidly moves the body forward, transitioning into the next motion cycle. In the swing phase, the foot of the right leg does not touch the ground when it swings forward, and the knee joint requires more significant movement. Therefore, there is a noticeable increase in knee joint angle variation during the swing phase compared to the support phase. The simulated results show that the trajectory of joint angle variations for the exoskeleton robot and human body essentially overlap, and the joint mobility of the exoskeleton robot remains within the range of joint mobility observed during human walking. Among them, the exoskeleton robot's hip joint and human hip joint are in close proximity to the actuator's starting point, showing the best synergy. Knee joint angles and ankle joint angles have some deviation only at the beginning of each gait cycle, but the deviation does not exceed 4° .This indicates that in terms of lower limb joint angle tracking, the human-machine system maintains excellent synergy.

In summary, based on the gait analysis, kinematic analysis, dynamic simulation, and human-machine synergy analysis, it can be concluded that the exoskeleton and human body movement patterns closely align with the expected preset trajectory, displaying alternating and repetitive characteristics. In the early stages of simulation, there is a minor fluctuation in the simulation curve due to momentary movements and the transition between left and right leg phases. However, overall, the exoskeleton robot operates smoothly, and the center of mass trajectories of each mechanism are smooth and exhibit good synergy with human movement. This suggests that the designed exoskeleton robot has a rational mechanical design, correct motor selection, and can meet the rehabilitation needs of lower limb walking.

5 Establishing the Human Gait Experimental Platform

5.1 Composition of the Kinematic Data Collection System

The optical motion capture system is designed based on passive infrared principles. The system's sampling frequency can be adjusted as needed and consists of 8 Mars1.3H motion capture cameras, with their parameters listed in Table 1[16-18]. These cameras are known for their high capture accuracy and low latency.The sampling frequency can be adjusted in real-time according to experimental requirements. The camera lenses have built-in image processors to ensure that the collected data is transmitted in real-time after cloud processing.

During experiments,efforts are made to arrange the cameras in a rectangular area. The tripod used for support is adjusted to its highest position to maximize the coverage of each camera, capturing the positions of markers comprehensively.

Tab. 1 *Parameters of Mars1.3H Motion Capture Cameras*

Mars1.3H	Parameter data
Image Resolution	1280*1024
Pixels	1.3MP
Frame Rate	240Hz
Latency	4.0ms
Lens Specifications	5.3mm
Field of View	56° ×46°
Three-Dimensional Accuracy	±0.2mm
Mars1.3H	Parameter data
Image Resolution	1280*1024

The rigid calibration kit consists of an L-shaped calibration rod and a T-shaped calibration rod. The L-shaped calibration rod establishes the coordinate system's origin and defines the positive directions of the x, y, and z axes for the entire system [19]. The T-shaped calibration rod is used for spatial calibration, and the calibration space size depends on the spatial range of motion for attaching markers to the human body, as shown in Fig 8.

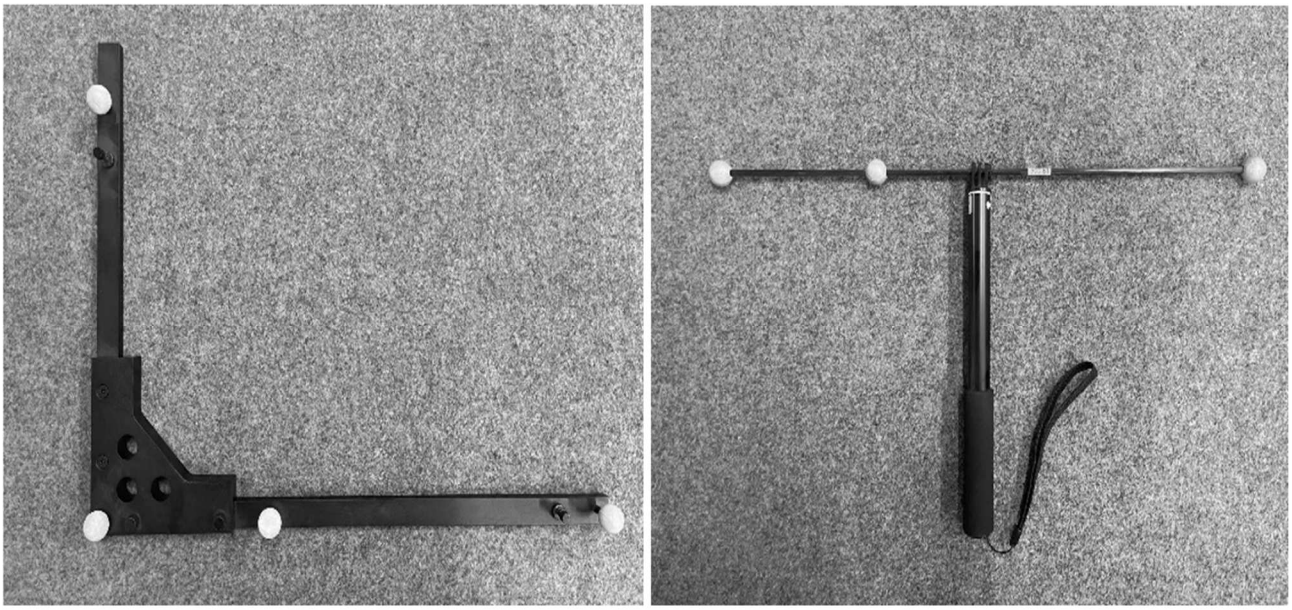

(a)L-shaped calibration rod (b)T-shaped calibration rod

Fig. 8 *Rigid Calibration Kit*

The dynamic data acquisition system used is the Bertec 4060 series three-dimensional force platform, as shown in Figure 9. It primarily serves the purpose of mechanical force measurement and analysis during human movement [20-22].

During measurement, the three-dimensional force sensors within the force platform integrate forces in the x, y, and z-axis directions into multiple channel data. Subsequently, data acquisition of the plantar forces is carried out using an NI acquisition card. Finally, the collected data is subjected to dynamic analysis using Seeker software. The main parameters of the system are as listed in Table 2.

Fig. 9 *Bertec 4060 Series Three-Dimensional Force Platform*

Tab. 2 *Three-Dimensional Force Platform Parameters*

FP4060-08-2000 force platform	Parameter data
Dimensions（mm）	600*400*83
Maximum Load（N）	Fx=Fy=5000, Fz=10000
Maximum Load（N·m）	Fx=3000, Fy=2500, Fz=1500
Natural Frequency（Hz）	Fx=Fy=340, Fz=550
Resolution（N/LSB）	±1
Linearity（FS）	0.2

When the force platform is in operation, the forces acting on the top plate are transmitted to the bottom plate through load sensors. Analyzing the sensor signals allows us to obtain the three-dimensional forces acting on the top plate. Ground reaction force is the vector sum of external forces in all directions, reflecting the ground forces experienced by the subject during walking. In summary, with all the systems set up, the overall human gait experimental platform looks as shown in Fig 10.

ISSN 1213–2489
e-ISSN 2787–9402

Fig. 10 *Human Gait Experimental Platform*

5.2 Gait Data Collection Experiment

After turning on the equipment, the first step is to calibrate the positions and angles of the cameras using the calibration device. Once calibration is complete, the gait data collection is tested to ensure there are no No.s. The coverage area of the detection zone can affect the cameras' ability to capture marker points. The participant enters the collection area, and you can observe the marker points in the simulated space, as shown in Fig 11. When the participant in the detection zone performs limb movements, the marker points move along with them. Use Seeker to check the camera capture status. You can select a single marker point to inspect if it has been recorded. It should ensure that each marker point is simultaneously captured by at least 3 cameras at any given moment, confirming sufficient coverage area to ensure data collection accuracy.

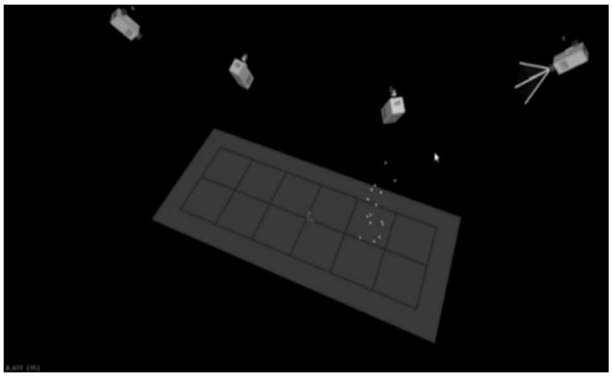

Fig. 11 *Camera Capture Ability Test*

After completing the testing, the gait data of the experimental subjects is collected. In this experiment, the experimental subjects have a height of 175cm and wear a professional motion capture suit to avoid optical noise from clothing during the experiment. 15 marker points are attached to the lower limbs of the experimental subjects, following the arrangement of the marker points according to the Helen Hayes model, as shown in Fig 12.

Fig. 12 *Helen Hayes Model and Lower Limb Marker Placement*

After correctly wearing the motion capture suit, the experimental subjects walk at a constant speed of 1 m/s along a straight line within an area with dimensions of [provide dimensions], as shown in Fig 13. The motion capture equipment captures and records the motion trajectories of the marker balls. Seeker is used to record the coordinates of the moving data points in the simulated space, and simultaneously, the ground reaction forces under the subjects' feet are recorded as they pass over the force platform. To ensure the stability and reliability of the experimental data, data from 100 walks by the experimental subjects within the area are recorded.

Fig. 13 *Experiment of Walking in a Straight Line on Flat Ground*

5.3 Gait Data Analysis

As shown in Fig 14, it represents the component of ground reaction force in the X-axis direction (forward direction of motion). Figure 15 shows the component of ground reaction force in the Y-axis direction (left-right direction of motion). Figure 16 displays the component of ground reaction force in the Z-axis direction (upward-downward direction).

You can see that the maximum ground reaction forces in the X, Y, and Z-axis directions are 200N, 100N, and 1300N, respectively. During the walking process, when the trailing leg provides maximum power, the other supporting leg begins to get involved in the movement, transitioning from the single-support phase to the double-support phase. The newly engaged leg helps to buffer the excess energy provided by the current limb, balancing it to maintain body stability. Subsequently, the vertical force of the leading leg rapidly decreases to zero as the foot leaves the force plate. So far, the first step of walking is completed, and the subsequent gait cycles will repeat this process, enabling continuous walking.

Throughout this process, the center of mass experiences no vertical acceleration only when the gravitational force acting on the subject equals the vertical ground reaction force on the force plate. In a normal-speed walking gait, there are two peak values in the vertical ground reaction force, one occurring during the impact-absorbing phase after ground contact and the other providing power for the next step. These two peak values are almost equal. During this period, the energy lost due to impact is replenished by muscle forces to sustain walking.

5.4 Experimental Results Comparative Analysis

The hip and knee joint angle changes in the human-machine coupled system simulation results and gait experiments are shown in Fig 17. In the figure, the solid black line represents the angle change curve in the simulation results, and the red dashed line represents the angle change curve in the gait experiments.

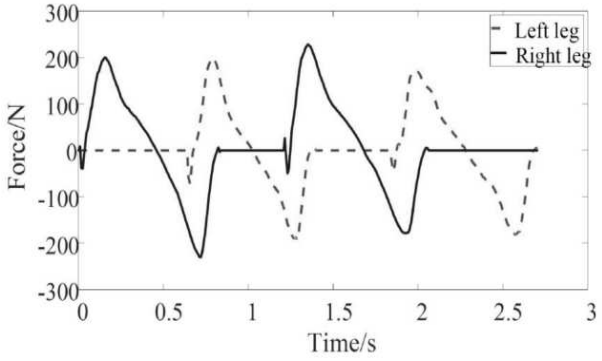

Fig. 14 *Component of Ground Reaction Force in the X-axis Direction*

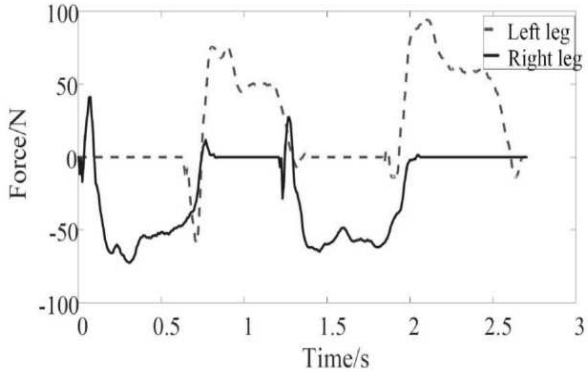

Fig. 15 *Component of Ground Reaction Force in the Y-axis Direction*

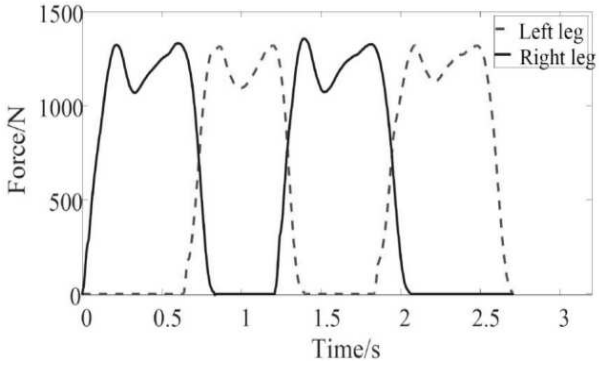

Fig. 16 *Component of Ground Reaction Force in the Z-axis Direction*

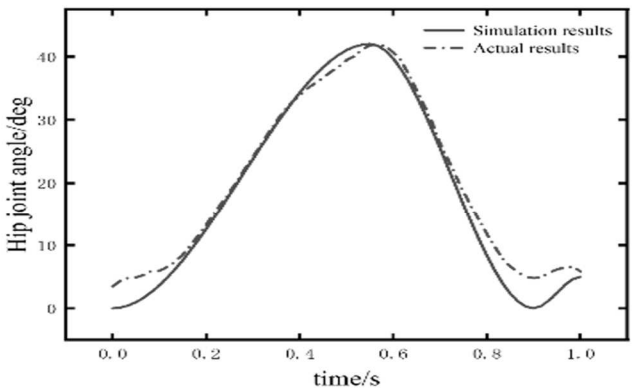

(a)Hip Joint

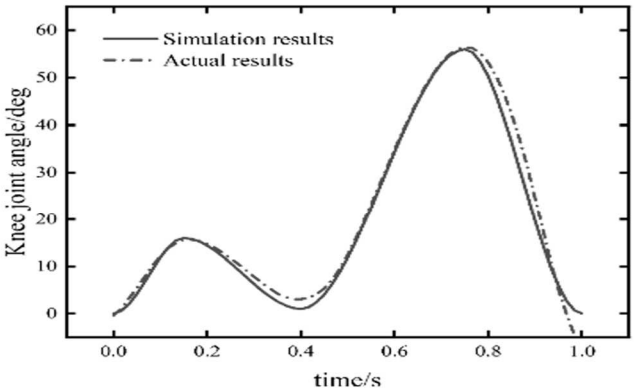

(b)Knee Joint

Fig. 17 *Hip and Knee Joint Angle Change Curves*

From Fig. 17, it can be observed that the simulated trajectory of the exoskeleton robot closely matches the normal gait trajectory of the human body. In the simulation results, the hip and knee joint ranges of motion of the exoskeleton robot do not exceed the range of motion observed during human walking. The hip and knee joint angles of the exoskeleton robot closely follow the kinematic patterns of the human body, with angle errors less than 3°.

In the simulation results, the knee joint angle changes of the exoskeleton robot closely match those of the human body. However, the hip joint angle changes between the two show better consistency during the 0.15 to 0.8 second time interval within the same gait cycle. The highest degree of overlap in hip joint angle occurs during the 0.2 to 0.7 second interval, while larger errors are observed during the 0 to 0.15 second and 0.8 to 1 second intervals. The main reason for this difference is that most of the structures in the virtual prototype simulation of the exoskeleton robot are set as rigid bodies, while the human hip joint exhibits complex gait trajectories at the beginning and end of the gait cycle, resulting in some discrepancies between the simulated hip joint angle changes and the experimental results.

6 Conclusion

This paper summarizes the work in four parts, including research proposal design, mechanical structure design, motion simulation and analysis, and experimental validation, with a focus on the movement reproduction and neural reshaping of lower limb mobility for individuals with lower limb disabilities. We proposed a human-machine coupling system that simulates the movement patterns of the human lower limbs and analyzed the motion characteristics of the human-machine coupling system and the synergy analysis of the human-machine system. The hip and knee joint angles of the exoskeleton robot were found to be in basic agreement with those of the human body, with angle errors less than 3° confirming that this configuration exhibits good agility in completing daily activities. Additionally, an experimental simulation platform was constructed for data collection and analysis of the human-machine system's movement, revealing the gait pattern changes in the human-machine system. This validates that the model can meet the rehabilitation needs of lower limb disabled individuals.

Acknowledgement

This work was supported by Shandong Key Research and Development Project (No.2019GHY112068, 2019GGX104102). Qingdao postdoctoral applied research project (A2020-070), the Natural Science Foundation of Shandong Province (No.ZR2020QE151) and Qingdao Huanghai University doctoral research Fund Project (2020boshi02).

References

[1] SHAH, R., SHAH, S. (2017). Delayed presentation or delayed diagnosis? A retrospective study of prospectively collected data of 482 foot and ankle injuries. In: *Injury*, Vol. 48, pp. 27-32. ISSN 0020-1383.

[2] ZHEN, A., HU, Y. Z. (2014). Diagnosis and repair of chronic ankle instability. In: *Chinese Journal of Tissue. Engineering Research*, Vol. 18, No. 9, pp. 1434-1440. ISSN 2095-4344.

[3] GREFKES, C., FINK, G. R. (2020). Recovery from stroke: Current concepts and futures perspectives. In: *Neurol. Res. Pract*, Vol. 2, pp. 17. ISSN 0161-6412.

[4] KHALID, Y. M., GOUWANDA, D., PARASURAMAN, S. (2015). A review on the mechanical design elements of ankle rehabilitation robot. Proceedings of the Institution of Mechanical Engineers. In: Part H: *Journal of Engineering in Medicine*, Vol. 229, No. 6, pp. 452-463. ISSN 0954-4119.

[5] LI., J., ZHANG,Z., TAO, C..(2017). A number synthesis method of the self-adapting upper-limb rehabilitation exoskeletons.In: *International Journal of Advanced Robotic Systems*, Vol. 14, No. 3, pp. 1-17. ISSN 1729-8814.

[6] ZHENG, J. J., SHEN, L. Y., DUAN, L R., DONG, X., QU, B., GAO, W., WU, H. (2020). Investigatation of Rehabilitation Human Resources in Shanghai.In: *China. Chin. J. Rehabil. Theory Pract*, Vol. 26, pp. 1471-1476. ISSN 1006-9771.

[7] ZHENG, Y., SONG, Q. J, LIU, J. X. (2019). Research on motion pattern recognition of exoskeleton robot based on multimodal machine learning model. In: *Neural Computing & Applications*. Vol. 32, No. 7, pp. 1869-1877. ISSN 0941-0643.

[8] DONG, M., ZHOU, Y., LI J. (2021). State of the art in parallel ankle rehabilitation robot: a systematic review. In: *Journal of NeuroEngineering and Rehabilitation*, Vol. 18, No. 1, pp. 1-15. ISSN 1743-0003.

[9] ZOU, Y., ZHANG, A., ZHANG, Q. (2022). Design and experimental research of 3-RRS parallel ankle rehabilitation robot. In: *Micromachines*, Vol. 13, No. 6, pp. 950. ISSN 2072-666X.

[10] LI, J.F., ZHANG K., ZHANG L.Y., ZHANG Z.K., ZUO S.P.(2019). Design and Kinematic Performance Evaluation of Parallel Ankle Rehabilitation Robot. In: *Journal of Mechanical Engineering*, Vol. 55, No. 9, pp. 29-39. ISSN 2329-8243.

[11] LIU, Q., ZUO, J., ZHU, C. (2021). Design and hierarchical force-position control of redundant pneumatic muscles-cable-driven ankle rehabilitation robot. In: *IEEE Robotics and Automation Letters*, Vol. 7, No. 1, pp. 502-509. ISSN 2377-3766.

[12] CONNER, B. C., SCHWARTZ, M. H., LERNER, Z. F. (2021). Pilot evaluation of changes in motor control after wearable robotic resistance training in children with cerebral palsy. In: J*ournal of biomechanics*, Vol. 126, pp. 1-18. ISSN 0021-9290.

[13] ALNAJJAR, F., ZAIER, R., KHALID, S. (2021). Trends and technologies in rehabilitation of foot drop: A systematic review. In: *Expert review of medical devices*, Vol. 18, No. 1, pp. 31-46. ISSN 1745-2422.

[14] SAGLIA, J. A., TSAGARAKIS, N. G., DAI, J. S. (2009). A High-performance Redundantly Actuated Parallel Mechanism for Ankle Rehabilitation. In: *The International Journal of Robotics Research*, Vol. 28, No. 9, pp. 1216-1227. ISSN 0278-3649.

[15] Du H. J., Yang G, Pei L. L. (2023). Design and Algorithm Research of a Weight Sorting Transport Robot. In: *Manufacturing Technology*. Vol. 23, No. 6, pp. 967-975. ISSN 1213-2489.

[16] ROSADO, W. M. A., VALDES, L. G. V., ORTEGA, A. B. (2017). Passive rehabilitation exercises with an ankle rehabilitation prototype based in a robot parallel structure. In: *IEEE Latin America Transactions*, Vol. 15, No. 1, pp. 48-56. ISSN 1548-0992.

[17] ZHENG, Y., WANG, Y. Q., LIU, J. X. (2021). Analysis and experimental research on stability characteristics of squatting posture of wearable lower limb exoskeleton robot. In: *Future Generation Computer Systems*, Vol. 125, No. 7, pp. 352-263. ISSN 1872-7115.

[18] Zhao H.F. (2023). Design of a Photoelectric Measuring Robot for Straightness of Deep/Blind Hole with Automatic Centering Function. In: *Manufacturing Technology*. Vol. 23, No. 5, pp. 739-749. ISSN 1213-2489.

[19] ROSADO, W. M. A., ORTEGA, A. B., VALDES, L. G. V. (2017). Active rehabilitation exercises with a parallel structure ankle rehabilitation prototype. In: *IEEE Latin America Transactions*, Vol. 15, No. 5, pp. 786-794. ISSN 1548-0992.

[20] YOO, D., SON, Y., KIM, D. H. (2018). Technology-Assisted Ankle Rehabilitation Improves Balance and Gait Performance in Stroke Survivors: A Randomized Controlled Study with 1-Month Follow-Up. In: *IEEE Transactions on Neural Systems and Rehabilitation Engineering*, Vol. 26, No. 12, pp. 2315-2323. ISSN 1558-0210.

[21] ZHENG, Y.,WANG, Y.Q.,LIU J.X.(2022).Research on structure optimization and motion characteristics of wearable medical robotics based on Improved Particle Swarm Optimization Algorithm. In: *Future Generation Computer Systems*, Vol. 129, No. 2022, pp. 187-198. ISSN 1872-7115.

[22] Wang S, Wu X.Y. (2023). Optimization and Experiment of Linear Motor Platform Servo Control Algorithm. In: *Manufacturing Technology*. Vol. 23, No. 6, pp. 999-1005. ISSN 1213-2489.

[23] AZCARAY, H., BLANCO, A., GARCIA, C. (2018). Robust GPI control of a new parallel rehabilitation robot of lower extremities. In: *International Journal of Control, Automation and Systems*, Vol. 16, No. 5, pp. 2384-2392. ISSN 2165-8285.

[24] KWOS S H, LEE B S, LEE H J, et al. (2020). Energy efficiency and patient satisfaction of gait with knee-ankle-foot orthosis and robot (ReWalk)-assisted gait in patients with spinal cord injury. In: *Annals of rehabilitation medicine*, Vol. 44, No. 2, pp. 131-141. ISSN 2234-0653.

[25] LAUBSCHER C A, GOO A, FARRIS R J, et al. (2022). Hybrid Impedance-Sliding Mode Switching Control of the Indego Explorer Lower-Limb Exoskeleton in Able-Bodied Walking. In: J*ournal of Intelligent & Robotic Systems*, Vol. 104, No. 4, pp. 76-80. ISSN 1573-0409.

[26] Song L, Sun H, Xu K.K., Shi X.Q., Zhou Y.Q. (2022). Path Planning under The Hull bottom of Painting Robot Based on Heuristic Multi-robot Cooperation in Ship Manufacturing. In: *Manufacturing Technology*. Vol. 22, No. 2, pp. 218-230. ISSN 1213-2489.